An Experimental Methodology to Characterise Post-Necking Behaviour and Quantify Ductile Damage Accumulation in Isotropic Materials

A. Sancho[a,c,*], M.J. Cox[a,b], T. Cartwright[b], C.M. Davies[a], P.A. Hooper[a], J.P. Dear[a,*]

[a] *Imperial College London, Department of Mechanical Engineering, London, SW7 2AZ, United Kingdom*
[b] *AWE Plc., Materials Science, Aldermaston, Reading, RG7 4PR, United Kingdom*
[c] *Now at University of Strathclyde, Advanced Forming Research Centre, Inchinnan, Renfrew, PA4 9LJ, United Kingdom*

Abstract

The development of ductile damage, that occurs beyond the point of necking in a tensile test, can be difficult to quantify. An experimental methodology has been developed to accurately characterise the post-necking deformation response of a material through continuous monitoring of the specimen's shape up until rupture. By studying the evolution of the neck geometry, the correct values of the local stress and strain have been determined in samples of grade 304L stainless steel and C110 copper. Notched bar specimens of various notch acuities were examined enabling the effects of stress triaxiality on ductile fracture to be determined. The methodology developed has provided a robust framework for macroscopic measurements of ductile damage during the necking process. To characterise the material degradation process, the elastic modulus reduction method was employed on hourglass-shaped specimens of the same materials. Stiffness degradation was measured using a small gauge extensometer during uninterrupted tensile tests with partial elastic unloadings. A metallographic study was conducted on progressively damaged specimens in order to validate the macroscopic damage measurements. A new non-linear ductile

*Corresponding authors
Email addresses: a.sancho15@imperial.ac.uk (A. Sancho), j.dear@imperial.ac.uk (J.P. Dear)

damage accumulation law has been developed and calibrated, which provides an advanced representation of the experimental results, and a significant improvement compared to linear accumulation models frequently employed. This realistic modelling approach considers the degradation of the material when it has undergone severe plastic deformation, and provides a more accurate representation of the near failure behaviour by considering the effects of stress triaxiality. The methodology provides accurate data for damage model development and calibration, to improve the predictions of remnant life from ductile damage in engineering components.

Keywords: Plasticity, Necking, Triaxiality, Ductile damage, Ductile fracture

1. Introduction

The ability to characterise very high strain deformation behaviour, and to quantify and predict ductile damage accumulation in a material is important for many engineering applications. For example, automotive industry designs its vehicles so that their bodywork plastically deforms, absorbing the energy of an impact. Components manufactured using metal forming experience very high plastic deformation, whilst avoiding failure by ductile damage. Hence models to describe the ductile damage accumulation to very high strains are required. Modern experimental and simulation techniques are capable of representing severe plasticity and material degradation, however, most constitutive laws employed in these models are obtained by conventional instrumentation, assuming uniform deformation through the sample, and thus limited to the stress-strain values at the point of strain localisation by necking.

The final stages of localised plastic deformation in the form of a neck in ductile isotropic materials were studied on round specimens by Bridgman (1964), who derived relationships between the geometry of the neck and the stresses and strains generated. These local stresses and strains represent the actual plastic behaviour of the material compared to a classical uniform tensile test approximation. With modern high resolution cameras, it is now possible to measure

and track accurately the curvature of the material in the necked region. High resolution imagining of the neck geometry combined with Bridgman (1964) theory, or a similar necking approximation, makes it possible to derive the stresses and strains in the centre of the neck, and hence the hardening behaviour to high strains. Rosa et al. (2003) performed studies on the neck development of metallic materials investigating alternative methods of neck characterisation without the need of geometry monitoring. Mirone (2004) further developed that approach proposing a material-independent necking model which required only the experimental true stress-strain curve and the neck onset strain to calculate the equivalent stress and equivalent strain. This analytical approach could be used as an alternative to the Bridgman model without the need of experimental profile curvature measurements. Other alternative approaches to consider the necking behaviour include the use of the virtual fields method to calculate post-necking hardening proposed by Kim et al. (2013); or the inverse methods based on Finite Element Model Updating (FEMU) (e.g. Kajberg and Lindkvist (2004); Koc and Stok (2004)). This technique consists of deducing the parameters of the model from its experimentally obtained solution. In the case of material necking, stain fields in the specimen surface can be measured using Digital Image Correlation (DIC), and finite elements simulations can be solved iteratively updating the model until the difference between the measured and estimated strain fields is minimised (Kajberg and Lindkvist (2004)).

Focusing on the methods that use the experimental measurement of the sample's profile, such as the Bridgman approach, several techniques have been proposed to record the shape of the specimen: G'Sell et al. (1992) used cameras to record the necking in polymers while Gerbig et al. (2016) opted for using Digital Image Correlation. Rittel et al. (2014) used high-speed cameras in Split Hopkinson Tensile Bar experiments to observe the necking of metals in dynamic conditions and Vaz-Romero et al. (2016) followed a similar approach to investigate the effect of multiaxiality in dynamic necks development. The expanding ring experiment is an alternative technique that can be used to quantify necking at even higher strain-rates ($\dot{\varepsilon} \sim 10^{-4} s^{-1}$), Zhang and Ravi-Chandar (2006).

The methodology proposed here makes use of Bridgman's approach but introduces a simplified method of neck profile measurement that requires just a single DSLR camera (Digital Single-Lens Reflex), and uses an automated image processing algorithm for neck extraction; therefore, it provides an effective and economical method to accurately characterise the necking phenomenon experimentally. The results obtained can be used to calibrate popular plasticity models such as Ramberg-Osgood (Ramberg and Osgood (1943)) and Johnson-Cook (Johnson and Cook (1983)), in addition to more complex models such as the mechanical threshold stress (MTS) model, which is based on dislocation theory (Mecking and Kocks (1981)), or the Bai and Wierzbicki (2008) model, which accounts for the effect of hydrostatic pressure and deviatoric stress.

The ability to characterise the shape of the neck allows the effects of stress triaxiality on the fracture behaviour of the material to be determined. Tensile tests on notched bars of different notched acuities are generally employed (see e.g. Bai and Wierzbicki (2008); Brünig et al. (2008)), to determine stress triaxiality effects on ductility. Stress triaxiality changes during the deformation process, however, when calibrating fracture models, the tensile ductility is associated with a single stress triaxiality ratio, which is effectively assumed constant during the test. In the past, the initial or final value of stress triaxiality was used for that purpose (Johnson and Cook (1985)). In more recent studies, the full history of the stress state obtained from finite elements simulations has generally been considered, e.g. Bai and Wierzbicki (2008). Considerable efforts have been made recently in an attempt to design ductile fracture experiments that produce locally proportional loading histories. In the methodology proposed here, the evolution of stress triaxiality along the test can be obtained experimentally. This is achieved by tracing the geometry of the neck, enabling the influence of stress state on ductility to be characterised, and enhancing the accuracy of ductile fracture models. Another parameter that is known to affect ductility of metals is Lode angle, which is related to the second and third invariants of the deviatoric stress tensor, and represents the type of loading that the material is undergoing (tension, compression, shear or a combination e.g.

mixed-mode loading). A wide variety of specimen geometries and experimental configurations have been proposed in order to study different combinations of stress triaxiality and Lode angle, e.g. cruciform and butterfly specimens, which were firstly proposed by Mohr and Henn (2007), and later used by other authors such as Xue and Wierzbicki (2008). However, the research presented here is focused on the study of stress triaxiality effects and Lode angle effects have not been analysed, therefore, only stress states similar to the ones studied can be represented at present by the methodology discussed in this paper.

Ductile damage accumulation rate, a measure of the plastic degradation of the material with plastic strain, has proven difficult to determine experimentally (Lemaitre and Dufailly (1987), Alves (2001)). Hence, very often a linear accumulation of damage rate is assumed. Various techniques have previously been proposed to calculate damage accumulation, all based on measuring a macroscopic mechanical property that is considered to be directly related to damage. The indirect methods include elastic modulus reduction measurements (Lemaitre and Dufailly (1987); Bonora et al. (2011)), hardness measurements (Oliver and Pharr (2004); Guelorget et al. (2007)), micro-structure analysis (Lemaitre and Dufailly (1987)), response to ultrasonic waves (Boccaccini and Boccaccini (1997); Kumar et al. (2010)), X-Ray micro-tomography (Cao et al. (2014)) and electric potential drop (Zhang et al. (2014)). In this work, an advanced stiffness reduction technique has been developed to measure damage. This features the use of a small extensometer, which combined with the aforementioned necking correction technique provides a fast and effective technique for damage quantification. The results obtained using this technique have been validated by observation of voids density from microstructural images of material that had undergone different levels of plastic deformation. An alternative approach to investigate damage accumulation rate would be to induce non-proportional paths during testing, and tune the adopted damage model according to the differences in terms of strain to fracture observed.

An aim of this study is to prove that damage accumulation is highly non-linear for most materials, as previously presented by Bonora et al. (2011). Dif-

ferent approaches exist to represent ductile damage and there are different opinions about its effect on material behaviour. Micro-mechanical models such as GNT (Gurson-Needleman-Tvergaard) (Needleman and Tvergaard (1984)) represent the actual processes of void nucleation, growth and coalescence involved in ductile damage. Continuum damage mechanics models like Bonora (1997) consider damage through its effects on macroscopic properties. These two approaches introduce a coupled modelling of damage, and include elastic and/or plastic softening of the material with ductile damage. Phenomenological models such as Johnson and Cook (1985) and Bai and Wierzbicki (2008) fit the fracture strain conditions to analytical expressions and generally assume a linear damage accumulation with no effect of damage on the elasto-plastic behaviour. A new, non-linear damage accumulation law is proposed here, which is based on the model proposed by Cortese et al. (2016) for non-proportional loading conditions, and also takes concepts from the continuum damage mechanics theory. This model can be used in simulations to calculate the level of material degradation, and can be coupled with the elasto-plastic calculations for a more realistic material representation. This new modelling approach has been carefully validated with appropriate experimentation.

2. Methodology

The materials and specimen geometries employed in this work are described below. The experimental methodologies developed for plasticity and damage assessment are also presented and the material models analysed. All the experiments discussed have been performed in quasi-static ($\dot{\varepsilon} \sim 10^{-3}$ s^{-1}) and room temperature conditions ($T \sim 20$ °C).

2.1. Materials

The behaviours of two different materials have been investigated, one an austenitic 304L stainless steel with low carbon (max. 0.03%) and minimum 18% chromium and 8% nickel contents; the other C110 copper, an alloy with

>99.90% copper content and oxygen generally below 0.04%. These materials have been selected due to their appreciable ductility and the availability of published work for comparison purposes.

2.2. Specimens

The test specimens were manufactured from rods in the as-drawn condition. Three different specimen geometries were used in this investigation: smooth round bars, notched round bars and hourglass shaped round bars. An image of the types of specimens tested is presented in Figure 1 and a summary of the dimensions of all the samples can be found in Table 1.

For plasticity and necking characterisation a conventional round bar specimen (RB) of 6 mm diameter and 30 mm gauge length as employed, as shown in Figure 2 (Test No. 1 in Table 1). For damage monitoring experiments, hourglass shaped specimens (HGR) were used (Figure 3, Test No. 2 in Table 1). The region of interest in these specimens is a central gauge region of uniform diameter 6 mm and length 6 mm, where damage will be concentrated. Above and below this region of interest the sample is tapered presenting a gradual narrowing, in order to avoid stress concentrations. The equal stress and deformation behaviour of RB and HGR specimens in their gauge section was verified with FE simulations. Similar geometries were used in the past for damage monitoring (Alves et al. (2000)) and necking analysis (Gerbig et al. (2016)).

Lastly, in order to study the effect of stress triaxiality on fracture strain, round notched bar specimens (RNB) with different notch acuities were used. Equation 1 can be derived from Bridgman's theory (Bridgman, 1964) and provides the initial value of stress triaxiality in the minimum cross section of the sample as a function of the geometry of the notch:

$$\eta = \frac{\sigma_H}{\bar{\sigma}} = \frac{1}{3} + \ln\left(1 + \frac{a}{\rho}\right) \tag{1}$$

where η is the stress triaxiality, σ_H the hydrostatic stress, $\bar{\sigma}$ the equivalent von Mises stress, a the cross-sectional radius in the notch and ρ the radius of curvature of the notch. Different notch geometries were tested to represent

various states of stress triaxiality (Tests No. 3-8 in Table 1), an example of which is shown in Figure 4.

2.3. Experimental procedure for plasticity modelling

A conventional tensile test is usually performed to determine the elastoplastic behaviour of materials using an extensometer to measure elongation and a load cell to obtain load. The true stress - strain performance of the material can then be derived from these measurements assuming uniform deformation behaviour using Equations 2 and 3:

$$\varepsilon_T = \ln(1 + \varepsilon_e) \tag{2}$$

$$\sigma_T = \sigma_e(1 + \varepsilon_e) \tag{3}$$

where σ_e and ε_e are the engineering stress and strain, and σ_T and ε_T the true stress and strain. The values obtained following this procedure are only valid while the material deforms uniformly, but the behaviour stops being uniform once localisation starts.

The experimental setup employed for the post-necking behaviour measurements during tensile tests can be seen in Figure 5, which includes a DSLR camera and a light source on each side of the sample. The camera used was a Nikon D7000 with 16.2 megapixel DX-format CMOS image sensor. The camera was carefully focused using a flat sheet located at the mid thickness position where the specimen was later placed, ensuring focus at the mid-plane of the specimen. By using a relatively large aperture (f/2), low exposure time (1/1000), low ISO (100), a focal length of 200 mm and an approximate distance to the sample of 600 mm the depth of field obtained was 0.5 mm, which is very narrow but assures that a sharp representation of the specimen's profile is obtained. The camera setup must not be moved after it has been calibrated, since with the narrow depth of field used small changes in the distance to the sample would lead to unacceptably blurry specimen edges in the images.

Additional lighting enables settings on the camera to be used that optimise the sharpness of the image, sacrificing its brightness. They also increase the

contrast between the specimen and the background making it easier to determine accurately the external profiles from the images. The specimen was painted white to improve contrast, as well as to avoid reflections from the metallic surface. The experiments are best performed soon after the samples have been painted so that the paint is still slightly wet, such that it is more likely to remain attached to the surface of the specimen. Generally, the tests were performed 1-2 hours after the specimens had been painted.

For profile sample extraction an image thresholding method was used. With this setup, the transition between the dark background of the image and the light region of the sample presents only 2-3 pixels of thickness with varying shades of grey, as observed in Figure 6. The equivalent size of each pixel can be obtained by comparing the actual diameter of the sample with the number of pixels across the specimen before the test, and in the case represented the side of each pixel measures 7.8 μm. If 3 pixels of dimensional uncertainty are considered for the thresholding method, the error of the profile measurement would be ≤ 23.4 μm, which can also be taken as the accuracy of the method.

The tests were conducted under quasi-static conditions ($\dot{\varepsilon} \sim 10^{-3}$ s^{-1}) in a conventional 250 kN tensile Instron machine. Images were recorded at a rate of 0.5 fps. This resulted in an average of 370 images taken along the stainless steel tests and 140 images along the copper tests, approximately 110 of which images corresponded to the necking region for both materials. An automated script was created to extract the specimen external profiles of each picture after having applied the threshold to the image. From the profiles, the minimum cross-sectional radius (a) and the fitted osculating circles radii (ρ) can be determined, as observed in Figure 7.

The theory derived by Bridgman (1964) can be used to obtain the true stress - true strain behaviour in the central point of the necked cross-section of the specimen. That is the location of interest for the present research, since the maximum value of stress triaxiality and ductile damage appears there during the localisation process, and being the aim to characterise damage, the most demanding conditions that first lead to fracture should be analysed. By mon-

itoring the minimum radius of the sample the average axial strain in the neck can be obtained using Equation 4 and the average axial stress with Equation 5:

$$\bar{\varepsilon} \approx \varepsilon_{zz,av} = 2 \ln \left(\frac{a_0}{a} \right) \tag{4}$$

$$\sigma_{zz,av} = \frac{Load}{\pi a^2} \tag{5}$$

where $\varepsilon_{zz,av}$ and $\sigma_{zz,av}$ represent the average strain and stress across the cross-section in the specimen axial direction, $\bar{\varepsilon}$ the equivalent strain, a_0 the initial cross-sectional radius and a the current cross-sectional radius. Bridgman model considers the assumptions that axial strain is uniform in the neck cross-section, and that proportional loading conditions take place. Under those assumptions, the radial and tangential strains are equal and double the magnitude of axial strain, therefore, the expression of Equation 4 corresponds also to the equivalent strain. The effect produced by the real distribution of variable strain in the cross-section was studied by Rosa et al. (2003) and Mirone (2004), but for this work, the level of accuracy provided by Bridgman's work has been considered acceptable.

Whilst axial strain varies very little across the neck even beyond necking, axial stress presents a radial variation that has to be taken into account. The material deforms uniformly before necking, and therefore, stress is also uniform. However, when necking starts the stress distribution has to be corrected and the axial stress at any radial position of the cross-section can be obtained using Equation 6:

$$\sigma_{zz} = \frac{\sigma_{zz,av}}{\left(1 + \frac{2\rho}{a}\right) \ln \left(1 + \frac{a}{2\rho}\right)} \left(1 + \ln \left(\frac{a^2 + 2a\rho + r^2}{2a\rho} \right) \right) \tag{6}$$

where σ_{zz} is the axial stress, $\sigma_{zz,av}$ the average axial stress, a the neck cross-sectional radius, ρ the neck radius of curvature and r the radial distance from the axis of the specimen. If the radial position studied is exactly the centre of the cross-section, the maximum axial stress is obtained. The expression obtained for the equivalent stress in the neck ($\bar{\sigma}$) following Bridgman approach is presented in Equation 7. Equivalent stress only depends on the geometry of the neck (a

and ρ) and the average axial stress, and it is the parameter that has been used to represent the material, along with the equivalent strain of Equation 4.

$$\bar{\sigma} = \frac{\sigma_{zz,av}}{\left(1 + \frac{2\rho}{a}\right) \ln\left(1 + \frac{a}{2\rho}\right)} \tag{7}$$

Round bar specimens (Figure 2) were used to obtain the equivalent stress - equivalent strain behaviour of the materials using the imaging method described above. The same sample geometry was also used to obtain the true stress - true strain of the material using a 6 mm gauge length extensometer and the classical processing method (Equations 2 and 3), in order to compare both techniques.

Additional tests were performed on hourglass round specimens (Figure 3), in which strain was measured using both techniques (the imaging and the extensometer). By doing this, calibration curves for the necking effect correction were produced. These curves associate each measurement of engineering strain and stress obtained from the extensometer and load cell to the value of equivalent strain and equivalent stress obtained from the neck geometry at that particular instant of the test. The calibration curves obtained are presented in Figure 8 for strains and stresses of stainless steel 304L and copper C110. As expected, the correction curves are lines of slope value ~ 1 before necking, since both methods yield the same results. When the neck develops, the slope increases in all the curves due to the localisation of stress and strain that is not captured by the traditional approach. While the increasing slope is easily observed for strains, a backwards or boomerang effect appears in the stress curves. Engineering stress starts decreasing passed the UTS, however, the real equivalent stress keeps increasing. The point of highest abscissa of these curves corresponds to the UTS point, after which localisation occurs with either equivalent stress increasing further up to failure (stainless steel, Figure 8c), or increasing and then decreasing back to zero, due to the material degradation (copper, Figure 8d). The calibration curves have later been used to account for the necking effects in the damage monitoring experiments.

2.4. Experimental procedure for ductile damage modelling

Two different experiments were performed in order to characterise ductile damage, one focused on the quantification of the material degradation when plastic strain is progressively applied, and the other on the ductile fracture strain at various states of stress triaxiality.

To determine the effect of stress triaxiality on fracture plastic strain, tensile tests on round notched bar specimens with different notch geometries were performed (Figure 4 represents a notch of 5 mm minimum diameter and 3 mm notch radius of curvature). The same equipment and room temperature conditions were used for these tests. The imaging technique described for plasticity assessment was also used to monitor the notch throughout the test. This has been especially useful, since it allows the evolution of the stress triaxiality in the centre of the notch to be calculated using the notch's geometrical parameters and Equation 1. The initial triaxiality of the specimen can be obtained from its initial geometry and Equation 1, however, this value varies along the test when the geometry of the notch changes, and the assumption of constant triaxiality would lead to inaccurate material modelling. From the stress triaxiality history, the average value at the centre of the neck was calculated as presented in Equation 8:

$$\eta_{av} = \frac{1}{\bar{\varepsilon}_f} \int_0^{\bar{\varepsilon}_f} \eta(\bar{\varepsilon}) d\bar{\varepsilon} \tag{8}$$

where η_{av} is the average stress triaxiality, $\eta(\bar{\varepsilon})$ the stress triaxiality history, $\bar{\varepsilon}$ the equivalent strain and $\bar{\varepsilon}_f$ the fracture equivalent strain. This average value has later been used for the calibration of models. Generally, fracture strain is obtained by measuring the diameter of the fractured specimen and comparing it with its initial value by means of Equation 4. For validation purposes the final diameter was also measured using a shadowgraph.

To measure the degradation that ductile damage produces in the material, the stiffness reduction method was employed. This technique consists of a tensile test which, instead of running continuously up to fracture, is partially unloaded at different plastic strain stages, and reloaded subsequently. This process is

exemplified in Figure 9. From the slope of each of the unloading cycles the damaged or effective elastic modulus ($\tilde{E}$) can be obtained, and from it, an estimation of damage expressed following the continuum damage mechanics definition:

$$D = 1 - \frac{\tilde{E}}{E} \tag{9}$$

where D is ductile damage, E the initial elastic modulus and $\tilde{E}$ the effective or deteriorated elastic modulus.

A 250 kN tensile Instron machine was used, in which the successive loading and unloading program was specified so that the test run in a continuous manner in quasi-static conditions ($\dot{\varepsilon} \sim 10^{-3}$ s^{-1}). The hourglass shaped specimens were used for these tests (Figure 3). To measure strain in the gauge region for later damage calculation, an extensometer of 6 mm gauge length and a maximum engineering strain measurement capability of 100% was used. In previous studies strain gauges were mainly used for accurate elastic modulus measurement (Bonora (1997); Lemaitre and Dufailly (1987); Alves et al. (2000)). Nevertheless, strain gauges are not able to measure more than 10% plastic strain before failing, and therefore, several test interruptions and gauge replacements were required, losing the origin of strain measurement and introducing great inaccuracy in the process. The alternative method used in this research can be performed in a continuous manner reducing considerably the test duration, the specimens preparation complexity and the potential imprecision of strain gauge replacement. Although strain gauges could potentially lead to a better approximation of the local strain values due to their smaller size, they cannot be attached accurately to an already necked geometry, which is the region of highest interest. The extensometer used in this research was smaller than those used in previous investigations (Bonora et al. (2011)), and while it still provides an averaged strain measurement in the necked region, a closer approximation to the more local measurement of a strain gauge was pursued. Another method to measure strain based on Digital Image Correlation instead of extensometer was initially considered, since it could potentially have led to an even better

approximation of the local strains in the neck, nevertheless, the method was discarded due to the higher scatter in the strains measured at such small scale (Sancho et al. (2016)).

The measurements obtained from the extensometer was used to create curves of stress vs. average strain in the gauge length, as shown in Figure 10, which represents an unloading and reloading cycle. The measured values of stress and strain were corrected with the curves presented in Figure 8 to account for the effects of necking. The unloading measurements were used to calculate elastic modulus, as suggested by Lemaitre and Chaboche (1990). The top and bottom 20% data of each unload cycle were omitted due to the non-linearities in the extremes and a fit was made to the linear region to determine the effective elastic modulus. By comparing this effective modulus with the initial value, ductile damage can be calculated using Equation 9.

As previously mentioned, the effects of cross-section reduction and necking on stress and strain have been taken into account. This has been done by interpolating the raw data obtained from the extensometer and load cell with the calibration curves of Figure 8 obtained from the plasticity tests, which relate measured engineering values with equivalent corrected values.

2.5. Plasticity and damage models

The experimental results obtained were used to calibrate the quasi-static and room temperature part of Johnson-Cook plastic and damage model (Johnson and Cook (1983, 1985)) with the new damage accumulation law proposed. Due to the quasi-static strain-rate and constant temperature of the experiments considered in this work, the models reduce to a power-law expression for plastic behaviour and an exponential expression for ductile damage, each of them with 3 parameters to be calibrated. Alternative models such as a classical power law for the plastic behaviour representation, and an exponential Rice and Tracey like model for the ductile fracture (each with only 2 parameters) could also be used. However, in this case the simplified versions of Johnson-Cook model were selected, as the work has been extended to different strain-rates and tem-

peratures (Sancho et al. (2018)). The hardening law is defined by Equation 10, where the first term represents the isotropic plastic strain hardening, the second term the strain-rate hardening and the third term the temperature softening:

$$\bar{\sigma} = \left[A + B\bar{\varepsilon}_{pl}^{n}\right]\left[1 + C\ln\left(\frac{\dot{\bar{\varepsilon}}_{pl}}{\dot{\bar{\varepsilon}}_{0}}\right)\right]\left[1 - \left(\frac{T - T_{ref}}{T_m - T_{ref}}\right)^{m}\right] \tag{10}$$

where $\bar{\sigma}$ represents the von Mises equivalent stress, $\bar{\varepsilon}_{pl}$ the equivalent plastic strain, $\dot{\bar{\varepsilon}}_{pl}$ the equivalent plastic strain-rate, $\dot{\bar{\varepsilon}}_{0}$ the reference strain-rate, T the temperature, T_m the melting temperature, T_{ref} the reference temperature and A, B, n, C and m the model parameters. Some authors use the room temperature as T_{ref} and others use the lowest temperature studied, hence care must be taken to keep consistent its definition.

To represent the ductile fracture point of the hardening curve, Johnson and Cook (1985) model has been used. The expression of fracture equivalent strain is similar to that of the flow rule with a term representing the effect of stress triaxiality on fracture, a second term the effect of strain-rate and a third term the effect of temperature:

$$\bar{\varepsilon}_{pl,f} = \left[D_1 + D_2\exp\left(D_3\eta\right)\right]\left[1 + D_4\ln\left(\frac{\dot{\bar{\varepsilon}}_{pl}}{\dot{\bar{\varepsilon}}_{0}}\right)\right]\left[1 + D_5\left(\frac{T - T_{ref}}{T_m - T_{ref}}\right)\right] \tag{11}$$

where $\bar{\varepsilon}_{pl,f}$ represents the fracture equivalent plastic strain, η the stress triaxiality, D_1, D_2, D_3, D_4 and D_5 the damage model parameters, and the strain-rates and temperatures have the same meaning as those in Equation 10.

In the original Johnson-Cook damage model a basic linear damage accumulation of the following form was presented:

$$D = \int_0^{\bar{\varepsilon}_{pl}} \frac{d\bar{\varepsilon}_{pl}}{\bar{\varepsilon}_{pl,f}} \tag{12}$$

Fracture was considered to occur when the accumulated damage reached a critical value of $D = 1$, i.e. when $\bar{\varepsilon}_{pl} = \bar{\varepsilon}_{pl,f}$.

After analysing the damage accumulation experimental results it has been concluded that this linear approximation does not represent the real behaviour of the studied materials and a different accumulation law has been proposed. It is based on Cortese et al. (2016) damage accumulation model that was derived

for ductile damage by making a direct parallelism with the high cycle fatigue damage law proposed by Palmgren (1924), but including also a non-linear power law for damage accumulation. For this work, Cortese model has been modified so that some concepts of continuum damage mechanics, such as critical damage (D_{cr}) and threshold plastic strain (ε_{th}), also appear in the equation:

$$D = D_{cr} \left(\frac{\bar{\varepsilon_{pl}} - \varepsilon_{th}}{\bar{\varepsilon}_{pl,f} - \varepsilon_{th}} \right)^{\frac{m}{\left(\bar{\varepsilon}_{pl,f}\right)^{q}}} \tag{13}$$

It includes an exponent which depends on the stress state through the fracture equivalent plastic strain ($\bar{\varepsilon}_{pl,f}$) and on the material by means of the model parameters m and q, $\bar{\varepsilon}_{pl}$ represents the accumulated equivalent plastic strain, ε_{th} the threshold plastic strain and D_{cr} the critical damage. The effect of varying the model parameters m and q is represented in Figure 11.

Consequently, the approach followed for damage and fracture modelling is mainly empirical, based on Johnson-Cook fracture model (Equation 11) and introducing a new non-linear damage accumulation law (Equation 13). This accumulation model is also of empirical nature, however, due the shape of the equation, some of its parameters represent actual physical behaviours of the material (threshold plastic strain and critical damage), the same as parameter A in Johnson-Cook plastic model (Equation 10) represents the yield stress. Therefore, one of the benefits of the proposed model is that it provides some additional information about the material damage whilst maintaining its empirical nature.

Some investigations have been conducted on the effect of stress state on the ductile damage accumulation law (Papasidero et al. (2015); Fincato and Tsutsumi (2019)). The model proposed here uses Johnson-Cook fracture criterion to calculate strain to fracture, which considers the effect of stress triaxiality, however, does not include the effect of Lode angle. Therefore, the model may not be able to represent the phenomena observed for stress states which are considerably different to the range analysed in this work. Nonetheless, this research is focused on the development of the experimental and modelling techniques required to measure and represent non-linear damage accumulation behaviours,

and the effect of a wider range of stress states could be analysed and included in the model in the future.

3. Experimental results

3.1. Uniaxial tests results

The equivalent plastic stress and strain behaviour of the material was determined by applying the neck monitoring technique described in Section 2.3. The results presented here correspond to Test No. 1 (see Table 1). From the images post-processing the history of specimen minimum radius (a) and neck radius of curvature (ρ) can be obtained. The evolution of these geometrical parameters is represented in Figure 12a for stainless steel 304L and in Figure 12b for copper C110.

As observed, the cross-sectional radius reduces approximately uniformly with applied strain for both materials. The other parameter represented is the neck radius of curvature, which presents an infinite value before necking starts due to the cylindrical geometry of the specimen. At the onset of necking this value decreases more or less quickly depending on how rapid the neck development is. Apart from the higher ductility and cross-section reduction of copper compared to stainless steel, the onset of necking location of both materials can be compared in Figure 12 and Table 2. While stainless steel presents a clear region of uniform plastic deformation up to $\sim$35% strain, copper necks almost from the beginning of the plastic region, allowing only $\sim$4% of strain before the instability starts. The values of final specimen cross-section measured with the shadowgraph are also included in Table 2, and it can be appreciated that the values are very similar to those obtained with the imaging method, validating the latter.

Making use of the geometrical parameters presented above, the equivalent stress - equivalent strain curve can be obtained. Figure 13a shows the results for stainless steel 304L, where results of two additional conventional tensile tests are also presented. For these last two tests, strain has been measured using an extensometer and Equations 2-3 have been used to post-process the results. As

expected, the results of both methods coincide before the specimen necks and the traditional approach cannot be used during necking, where the real stress and strain are no longer uniform. The same results are presented for copper C110 in Figure 13b, where a conventional tensile test has also been plotted. The outcome is the same as that of the stainless steel, being in this case even more pronounced due to the early necking of copper. The plastic strain - stress obtained for this material using Equations 2-3 is inappropriate, since it necks almost from the beginning of the test. The fracture mode is also different in both materials, while the stainless steel fails suddenly when it reaches its failure strain, the copper fails progressively with high ductility, hence the gradual stress decrease observed in Figure 13b.

3.2. Triaxiality effects results

The effect of stress triaxiality on ductility has been studied by testing round notched bar specimens with different notch geometries. The results correspond to Tests No. 3 - 8 of Table 1, but results of Test No. 1 are also included here, since they represent the extreme case of a notch with an infinite notch radius.

The same imaging methodology previously presented for smooth specimens has been employed here for the analysis of the notched specimens. Tracking the curvature of the neck, present from the beginning in these specimens, the evolution of the geometrical parameters a (cross-sectional radius) and ρ (neck radius of curvature) has been obtained. The neck reduction as a function of equivalent plastic strain is governed by Equation 4, and results in an exponentially decreasing curve that only differs for each specimen geometry on the fracture strain point, which becomes smaller for higher triaxialities.

The evolution of the other parameter, the neck radius of curvature, is presented in Figure 14a for the stainless steel and Figure 14b for the copper. Both materials follow similar trends, presenting small curvature variation the sharper notches (almost no variation for stainless steel) and considerable curvature decrease the smoother geometries. The curvature at fracture is slightly smaller for the copper compared to the stainless steel. For each of the materials all the

specimens fail at similar values of curvature, with a weak ascending trend for decreasing triaxialities.

The equivalent stress - equivalent strain curves of all the tests conducted and obtained using the imaging method and Bridgman theory are presented in Figure 15a for stainless steel 304L and Figure 15b for copper C110. In Figures 14-15 the yellow curves correspond to the round bar tensile test (Test No. 1), and have been previously presented in Figure 12 for radius of neck cross-section and radius of curvature and in Figure 13 for stress-strain. The rest of curves depict the different notch geometries tested with the expected trend of decreasing fracture equivalent strain for increasing triaxiality already observed in the a and ρ plots. In Figure 15 it can be observed that all the curves have the same yield stress and hardening rate, proving that stress triaxiality does not affect the early plastic region, and only affects the final fracture conditions. A difference is observed in the plastic strain for which copper starts undergoing severe degradation, which follows the same trend as fracture strain, appearing earlier the higher the stress triaxiality.

If the maximum axial stress is analysed (Figure 16), it can be observed that most stainless steel specimens fracture at a similar maximum axial stress value, independently of the stress triaxiality. In the case of copper, it is the initiation of the severe degradation process which occurs at the maximum axial stress of the material, while instead of failing in a brittle manner, a subsequent degradation occurs before final fracture. The value of maximum axial stress in the centre of the neck is therefore, in both cases, the physical limit that the material can withstand in tensile conditions and is not affected by stress triaxiality.

From a damage modelling point of view, it is well known that fracture equivalent strain decreases exponentially with stress triaxiality (Johnson and Cook (1983); Bai and Wierzbicki (2008)); however, the results of this investigation are presented in Figure 17, where the stress triaxiality history of each specimen obtained with the imaging method has also been plotted. The crosses represent the fracture strain conditions against the average stress triaxiality throughout the test, which in some cases varies considerably. The curves for stainless steel

are smooth up to fracture while the copper results present some fluctuation at the end. This occurs because the neck developed by the steel presents a smooth curvature during the whole deformation process; the neck of the copper specimens, however, is much sharper at the last stages of plastic deformation, making it very difficult to determine the curvature. If the yellow lines obtained from the smooth samples are analysed, it can be observed that although that geometry is generally used to represent uniaxial conditions, these are only met during the uniaxial deformation region, and a considerable increase of stress triaxiality takes place afterwards.

The selection of a stress triaxiality value for the test supposes a difficulty for fracture models calibration. In some works the initial or final stress triaxialities have been used, nonetheless, this implies a large error for some geometries and, since in this case the triaxiality history is known, the use of the average triaxiality given by Equation 8 has been considered the most adequate alternative. This approach was already used by Wierzbicki et al. (2005), making use in that case of calibrated finite elements simulations to estimate the stress triaxiality evolution, and thus the average triaxiality.

Detailed results with the information presented in Figure 17 are also available in Tables 3 and 4 for stainless steel and copper respectively. For each specimen the theoretical value of stress triaxiality predicted by Equation 1 is firstly shown. Since this value changes through the experiment, the values of initial, final and average triaxiality calculated with the imaging method are presented. Finally, the fracture equivalent strain obtained also with the imaging technique is shown. The same value obtained from the post-test specimen diameter measurement using a Starret HE400 optical comparator and Equation 4 is also displayed for comparison and validation of the imaging methodology.

3.3. Damage accumulation results

The outcome of the last experiment conducted is the evolution of ductile damage accumulated as the equivalent plastic strain progresses for the uniaxial loading case. These results complement those of the fracture conditions by

characterising the degradation process that occurs between damage initiation and final fracture. They correspond to Test No. 2 of Table 1, for which the hourglass shaped specimen geometry has been used.

The effective elastic modulus measurement method with a small extensometer, as previously described, has been used to obtain the results presented in Figure 18. The results of four stainless steel 304L specimens are shown in Figure 18a and those of three copper C110 specimens in Figure 18b. As observed, the repeatability of results is quite good in the case of stainless steel, with a maximum standard deviation of all the elastic modulus measurements taken at a particular plastic strain of 3.04 GPa, and an average standard deviation of the measurements taken at differnet plastic strains of 0.86 GPa. The results display a similar shape to that presented in Bonora et al. (2011) for another steel. For copper, the results show a bigger scatter (maximum standard deviation of 3.31 GPa and average standard deviation of 1.53 GPa in the measurement of elastic modulus), and the trend observed is clearly different to that of the stainless steel. A very similar material was also studied in Lemaitre and Dufailly (1987) and Bonora et al. (2011), and the behaviour reported is in close agreement with that obtained in the present research.

The stainless steel shows a prominent initial increase of damage that progressively stabilizes to a quite low critical damage value (the same behaviour has been observed in microstructural measurements, as will be presented in the following section). For copper, damage does not appear at the early stages of deformation and then increases fairly linearly. This exemplifies the different damage accumulation behaviours that diverse materials can present and the requirement of a non-linear damage growth model that allows to modify the shape of the accumulation. The appearance of ductile damage at initial stages of plasticity is generally associated to the nucleation of voids due to the fracture of hard particles within the material, therefore, the results suggest that these defects appear in stainless steel 304L as soon as plastic deformation is applied, however, some plastic strain can be applied to copper C110 before damaging the material.

For copper, it can be observed in Figure 18b that there are no damage measurements beyond an equivalent plastic strain of around $\bar{\varepsilon}_{pl} = 1$. This is because from that point onwards the material is so degraded, as observed in Figure 13b, that unloading and reloading cycles cannot be performed without fracturing the specimen; therefore, damage has only been measured up to the severe degradation start point and not until final fracture conditions.

3.4. Microstructural analysis

A second experimental method has been applied to measure damage and validate the experimental results obtained with the elastic modulus reduction technique. This has consisted in the analysis of internal porosity in the minimum cross-section of specimens with the same geometry of those used for the elastic modulus analysis (HGR6, see Figure 3) strained to different levels of plastic deformation. It has been achieved through a metallographic study of six stainless steel 304L specimens that have been plastically deformed to the plastic strain levels specified in Table 5. The samples were deformed in the same quasi-static and room temperature conditions used to obtain the elastic modulus results. After being strained, the central region of the specimens was cut using a Struers Accutom-5 high precision cut-off machine, mounted and polished using an ATA Saphir 520 semi-automatic polisher down to 0.1 µm using OP-S colloidal silica suspension as the final stage. A Zeiss compound optical microscope has been used to take pictures of their microstructure. The main objective of the investigation has been to quantify the porosity or void density in the micrographs, defined as percentage of the total area occupied by voids. A thresholding algorithm was programmed in Matlab to batch process the images from the microscope, and measurements of porosity have been taken in different locations of the specimen's cross-section.

Dark-field microscopy is recommended to detect voids, since the images have provided an improved contrast, making it easier to differentiate the defects from the material during the thresholding process. A square region of size 156 µm x 156 µm in the centre of the picture was analysed in order to avoid brightness and

contrast peaks from the corners. The threshold value used in the images post-processing was calibrated by analysing the zoomed-in image of individual voids, both in the original and the thresholded picture. Their size has been compared and the threshold modified until the size of both voids has been reasonably similar, as shown in Figure 19.

The post-process of micrographs has provided the porosity contour maps in the neck cross-section of Figure 20, where the first sample corresponds to the undamaged raw material, and the other six to the strained samples presented in Table 5. In these plots, the final diameters of all samples are proportional to the real values and the colour scale is also the same in all of them except in the last one, which presents much higher void density than the rest. From the analysis it was observed that the porosity distribution in the raw material is almost perfectly uniform, of very low value, and can be attributed to the inherent defects present in the material. Porosity is also fairly uniform in the cross-section of the following four specimens, the lighter blue in the porosity contours represents the higher void density, nevertheless, porosity increases significantly for specimen # 34 ($\bar{\varepsilon}_{pl} = 0.11$), and almost stabilises for the following three specimens, validating the behaviour observed from the elastic modulus measurements. Finally, the last two specimens were deformed beyond the necking limit, presenting a much higher porosity in general, and a higher concentration in the centre of the specimen than near its surface, especially specimen # 6, which had already fractured.

The porosity results of the contour plots have been plotted together in Figure 21, where the evolution of void density along the plastic range can be analysed. For each sample, the average of all the measurements taken in the cross-section has been represented. As observed, the trend is the same described above, with a significant increase of porosity in the first stages of plastic deformation, and a subsequent stabilisation and slight increase near fracture. The mean values of ductile damage from Figure 18a obtained by measuring changes in elastic modulus have also been included. Although the scale is different for the void density and the macroscopic damage, it can be observed that both mea-

surements follow the same trend. These results prove that the ductile damage measured from elastic modulus degradation is driven by voids nucleation, growth and coalescence. However, they also suggest that the reduction of mechanical properties does not take exactly the same value as the area reduction that these voids produce in the cross-section, as is generally asserted by continuum damage mechanics formulation. Therefore, additional degradation processes linked to the density of voids, but not entirely to the area that they occupy, have to be responsible of the reduction of material properties and will be studied in the future. From the degradation of elastic modulus, which is an actual macroscopic quantifiable property, a value of ductile damage can be obtained and used in material models to perform useful engineering calculations. The microscopic analysis carried out in this section serves as validation of the trends followed by the ductile damage parameter, but it is considered that the elastic modulus approach can provide a more real representation of the real macroscopic operation of components.

4. Model calibration

The equivalent stress - equivalent strain results obtained through the imaging technique applied to tensile specimens (Figure 13) have been used to calibrate the isotropic hardening part of Johnson-Cook plastic model (Equation 10), to represent the plastic behaviour of the studied materials. The experimental stress - strain results and the fitted plastic model curve are presented in Figure 22 and the model parameters obtained summarised in Table 6. The fracture equivalent plastic strain - stress triaxiality results of Figure 17 have been used to calibrate the quasi-static and room temperature part of Johnson-Cook fracture model (Equation 11). The experimentally obtained data points as well as the model fitted curve and the model parameters for stainless steel 304L and copper C110 are represented in Figure 23. In a similar manner, the results obtained in the damage accumulation experiments (Figure 18) have been fitted to the proposed damage accumulation law of Equation 13.

In this case damage evolves with equivalent plastic strain ($\bar{\varepsilon}_{pl}$) and with fracture equivalent plastic strain, and hence with stress triaxiality ($\bar{\varepsilon}_{pl,f} = f(\eta)$), according to the non-linear model. The variables to be calibrated based on the experimental evidence are D_{cr}, ε_{th}, q and m, as well as the variables of Johnson-Cook model embedded in the fracture equivalent plastic strain expression (D_1, D_2 and D_3). The experimental damage points can be fitted to a three dimensional surface against equivalent plastic strain and stress triaxiality axes ($D = f(\bar{\varepsilon}_{pl}, \eta)$), as presented in Figure 24. The crosses represent the damage - equivalent plastic strain values already plotted on Figure 18, while the triaxiality data has been obtained from the neck monitoring technique, following a similar procedure to that used to obtain the engineering to equivalent strain corrections.

The parameters D_1, D_2 and D_3 of Johnson-Cook model have been calibrated by least squares fitting of the fracture experimental data (fracture equivalent plastic strain vs. average stress triaxiality throughout the experiment) to Equation 11. D_{cr}, ε_{th}, m and q of the accumulation law have also been obtained by least squares fitting of the damage accumulation data to Equation 13 using the previously fitted Equation 11 expression as input. The calibrated variables obtained for both materials have been summarised in Table 7.

5. Conclusions

The proposed advanced methodology was successfully employed to obtain the post-necking equivalent stress - strain measurements of 304L stainless steel and C110 copper. The accuracy of the approach was validated by comparison with traditional tensile results in the uniform deformation region and with post-fracture geometrical measurements. The technique was applied using affordable equipment, making it accessible and of high value for industrial applications.

The measurements of stress triaxiality demonstrated that this parameter changes considerably throughout the tests, highlighting the fact that a constant value cannot be assumed. In this research, the use of the average measured

value is proposed as a way of accounting for the variation of stress triaxiality when calibrating the fracture model.

A highly non-linear ductile damage behaviour was measured on 304L stainless steel and C110 copper. Additionally, these materials showed significant differences in their damage accumulation behaviour. The above findings demonstrated the need of a complex and versatile ductile damage model that is able to represent non-linearity and different damage accumulation shapes.

The damage accumulation behaviour was validated by a microstructural analysis, which provided estimations of porosity or void density along the plastic deformation process. The trends followed by the increase in void density and the degradation of elastic modulus are coincident. However, the magnitude of modulus decrease is much higher than that of porosity increase, suggesting that void density does determine the shape of damage accumulation, but additional degradation phenomena proportional to void density occur within the material and require further investigation.

The proposed ductile damage model includes non-linear behaviour and has been successfully calibrated using the experimental data gathered. The capability of representing accurately damage accumulation makes the model an effective solution in, for example, the automotive and transport industry, where accurate damage prediction in collisions is important for safe and efficient component design. Also, the approach is of much value to components manufactured using metal forming where very high plastic deformation can occur and there is a need to avoid failure by ductile damage.

Acknowledgement

The financial and technical support received from AWE Plc. is very much appreciated for this research.

References

Alves, M., 2001. Measurement of ductile material damage. Mechanics of Structures and Machines 29, 451–476. doi:10.1081/SME-100107622.

Alves, M., Yu, J., Jones, N., 2000. On the elastic modulus degradation in continuum damage mechanics. Computers & Structures 76, 703–712. doi:10.1016/S0045-7949(99)00187-X.

Bai, Y., Wierzbicki, T., 2008. A new model of metal plasticity and fracture with pressure and Lode dependence. International Journal of Plasticity 24, 1071–1096. doi:10.1016/j.ijplas.2007.09.004.

Boccaccini, D., Boccaccini, A., 1997. Dependence of ultrasonic velocity on porosity and pore shape in sintered materials. Journal of Nondestructive Evaluation 16, 1–6. doi:10.1023/A:1021891813782.

Bonora, N., 1997. A nonlinear CDM model for ductile failure. Engineering Fracture Mechanics 58, 11–28. doi:10.1016/S0013-7944(97)00074-X.

Bonora, N., Ruggiero, A., Gentile, D., De Meo, S., 2011. Practical applicability and limitations of the elastic modulus degradation technique for damage measurements in ductile metals. Strain 47, 241–254. doi:10.1111/j.1475-1305.2009.00678.x.

Bridgman, P., 1964. Studies in Large Plastic Flow and Fracture. 2nd ed., Harvard University Press, Cambridge, Massachusetts.

Brünig, M., Chyra, O., Albrecht, D., Driemeier, L., Alves, M., 2008. A ductile damage criterion at various stress triaxialities. International Journal of Plasticity 24, 1731–1755. doi:10.1016/J.IJPLAS.2007.12.001.

Cao, T.S., Maire, E., Verdu, C., Bobadilla, C., Lasne, P., Montmitonnet, P., Bouchard, P.O., 2014. Characterization of ductile damage for a high carbon steel using 3D X-ray micro-tomography and mechanical tests - Application to

the identification of a shear modified GTN model. Computational Materials Science 84, 175–187. doi:10.1016/j.commatsci.2013.12.006.

Cortese, L., Nalli, F., Rossi, M., 2016. A nonlinear model for ductile damage accumulation under multiaxial non-proportional loading conditions. International Journal of Plasticity 85, 77–92. doi:10.1016/j.ijplas.2016.07.003.

Fincato, R., Tsutsumi, S., 2019. Numerical modeling of the evolution of ductile damage under proportional and non-proportional loading. International Journal of Solids and Structures 160, 247–264. URL: https://doi.org/10.1016/j.ijsolstr.2018.10.028, doi:10.1016/j.ijsolstr.2018.10.028.

Gerbig, D., Bower, A., Savic, V., Hector, L.G., 2016. Coupling digital image correlation and finite element analysis to determine constitutive parameters in necking tensile specimens. International Journal of Solids and Structures 97_98, 496–509. doi:10.1016/j.ijsolstr.2016.06.038.

G'Sell, C., Hiver, J., Dahoun, A., Souahi, A., 1992. Video-controlled tensile testing of polymers and metals beyond the necking point. Journal of Materials Science 27, 5031–5039. doi:10.1007/BF01105270.

Guelorget, B., François, M., Lu, J., 2007. Microindentation as a local damage measurement technique. Materials Letters 61, 34–36. doi:10.1016/j.matlet.2006.03.146.

Johnson, G.R., Cook, W.H., 1983. A constitutive model and data for metals subjected to large strains, high strain rates and high temperatures, in: Proceedings of the 7th International Symposium on Ballistics, pp. 541–547.

Johnson, G.R., Cook, W.H., 1985. Fracture characteristics of three metals subjected to various strains, strain rates, temperatures and pressures. Engineering Fracture Mechanics 21, 31–48. doi:10.1016/0013-7944(85)90052-9.

Kajberg, J., Lindkvist, G., 2004. Characterisation of materials subjected to large strains by inverse modelling based on in-plane displacement fields. In-

ternational Journal of Solids and Structures 41, 3439–3459. doi:10.1016/j.ijsolstr.2004.02.021.

Kim, J., Serpantié, A., Barlat, F., Pierron, F., Lee, M., 2013. Characterization of the post-necking strain hardening behavior using the virtual fields method. International Journal of Solids and Structures 50, 3829–3842. doi:10.1016/j.ijsolstr.2013.07.018.

Koc, P., Stok, B., 2004. Computer-aided identification of the yield curve of a sheet metal after onset of necking. Computational Materials Science 31, 155–168. doi:10.1016/j.commatsci.2004.02.004.

Kumar, A., Torbet, C., Pollock, T., Wayne Jones, J., 2010. In situ characterization of fatigue damage evolution in a cast Al alloy via nonlinear ultrasonic measurements. Acta Materialia 58, 2143–2154. doi:10.1016/J.ACTAMAT.2009.11.055.

Lemaitre, J., Chaboche, J., 1990. Mechanics of Solid Materials. Cambridge University Press, Cambridge.

Lemaitre, J., Dufailly, J., 1987. Damage measurements. Engineering Fracture Mechanics 28, 643–661. doi:10.1016/0013-7944(87)90059-2.

Mecking, H., Kocks, U., 1981. Kinetics of flow and strain-hardening. Acta Metallurgica 29, 1865–1875. doi:10.1016/0001-6160(81)90112-7.

Mirone, G., 2004. A new model for the elastoplastic characterization and the stress – strain determination on the necking section of a tensile specimen. International Journal of Solids and Structures 41, 3545–3564. doi:10.1016/j.ijsolstr.2004.02.011.

Mohr, D., Henn, S., 2007. Calibration of stress-triaxiality dependent crack formation criteria: A new hybrid experimental-numerical method. Experimental Mechanics 47, 805–820. doi:10.1007/s11340-007-9039-7.

Needleman, A., Tvergaard, V., 1984. An analysis of ductile rupture in notched bars. Journal of the Mechanics and Physics of Solids 32, 461–490. doi:10.1016/0022-5096(84)90031-0.

Oliver, W., Pharr, G., 2004. Measurement of hardness and elastic modulus by instrumented indentation. Advances in understanding and refinements to methodology. Materials Research Society 19, 3–20. doi:10.1557/jmr.2004.19.1.3.

Palmgren, A., 1924. Die lehensdauer von kugellagern 68, 339–341.

Papasidero, J., Doquet, V., Mohr, D., 2015. Ductile fracture of aluminum 2024-T351 under proportional and non-proportional multi-axial loading: Bao-Wierzbicki results revisited. International Journal of Solids and Structures 69-70, 459–474. URL: http://dx.doi.org/10.1016/j.ijsolstr.2015.05.006, doi:10.1016/j.ijsolstr.2015.05.006.

Ramberg, W., Osgood, W., 1943. Description of stress-strain curves by three parameters. Technical Report. NASA Science and Technical Information Facility, Technical Note No. 902.

Rittel, D., Rotbaum, Y., Rodriguez-Martinez, J., Sory, D., Zaera, R., 2014. Dynamic necking of notched tensile bars : An experimental study. Experimental Mechanics 54, 1099–1109. doi:10.1007/s11340-014-9860-8.

Rosa, G., Mirone, G., Risitano, A., 2003. Postnecking elastoplastic characterization : degree of approximation in the Bridgman method and properties of the flow-stress/true-stress ratio. Metallurgical and Materials Transactions A 34A, 615–624.

Sancho, A., Cox, M., Cartwright, T., Aldrich-Smith, G., Hooper, P., Davies, C., Dear, J., 2016. Experimental techniques for ductile damage characterisation. Structural Integrity Procedia 2, 966–973. doi:10.1016/j.prostr.2016.06.124.

Sancho, A., Cox, M., Hooper, P., Cartwright, T., Davies, C., Dear, J., 2018. Effects of strain rate and temperature on ductile damage of metals. Proceedings of the ASME 2018 Pressure Vessels and Piping Conference, Prague, Czechia , PVP2018–85158doi:10.1115/pvp2018-85158.

Vaz-Romero, A., Rotbaum, Y., Rodríguez-Martínez, J., Rittel, D., 2016. Necking evolution in dynamically stretched bars: New experimental and computational insights. Journal of the Mechanics and Physics of Solids 91, 216–239. URL: http://dx.doi.org/10.1016/j.jmps.2016.02.024, doi:10.1016/j.jmps.2016.02.024.

Wierzbicki, T., Bao, Y., Lee, Y.W., Bai, Y., 2005. Calibration and evaluation of seven fracture models. International Journal of Mechanical Sciences 47, 719–743. doi:10.1016/j.ijmecsci.2005.03.003.

Xue, L., Wierzbicki, T., 2008. Ductile fracture initiation and propagation modeling using damage plasticity theory. Engineering Fracture Mechanics 75, 3276–3293. doi:10.1016/j.engfracmech.2007.08.012.

Zhang, H., Ravi-Chandar, K., 2006. On the dynamics of necking and fragmentation - I. Real-time and post-mortem observations in Al 6061-O. volume 142. doi:10.1007/s10704-006-9024-7.

Zhang, S., Xia, Q., Li, W., Zhou, X., 2014. Ductile damage measurement and necking analysis of metal sheets based on digital image correlation and direct current potential drop methods. International Journal of Damage Mechanics 23, 1133–1149. doi:10.1177/1056789514527978.

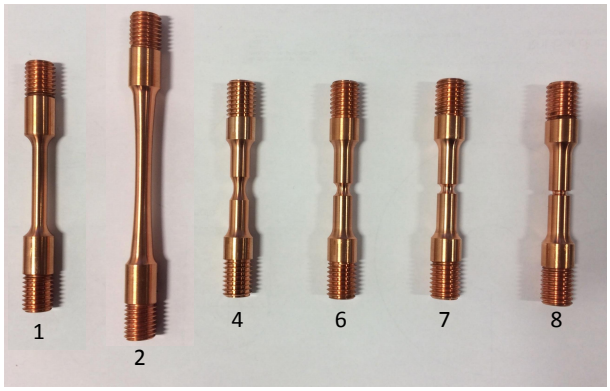

Figure 1: Geometry of copper specimens tested (for stainless steel, specimens 3 and 5, as defined in Table 1, have been used instead of specimen 4).

Test number	Specimen characteristics	Notch acuity, a/ρ [-]	Curvature, ρ [mm]	Diameter, $2a$ [mm]	Theoretical triaxiality, η_0 [-]
1	Smooth bar	0	∞	6	0.333
2	Hourglass shaped bar	0	∞	6	0.333
3	Notched bar	0.25	8	4	0.557
4		0.313	8	5	0.605
5		0.417	6	5	0.682
6		0.833	3	5	0.940
7		1.25	2	5	1.144
8		2.5	1	5	1.586

Table 1: Characteristics of the analysed specimens.

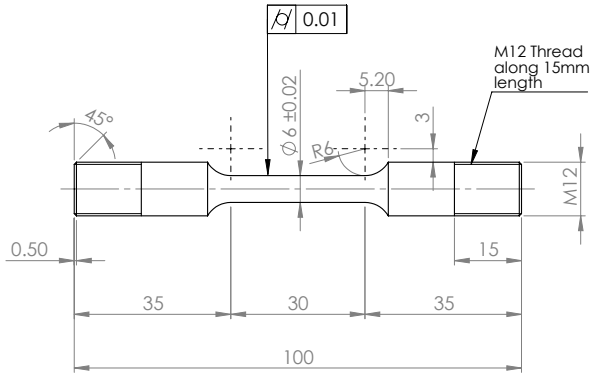

Figure 2: RB6 specimen geometry.

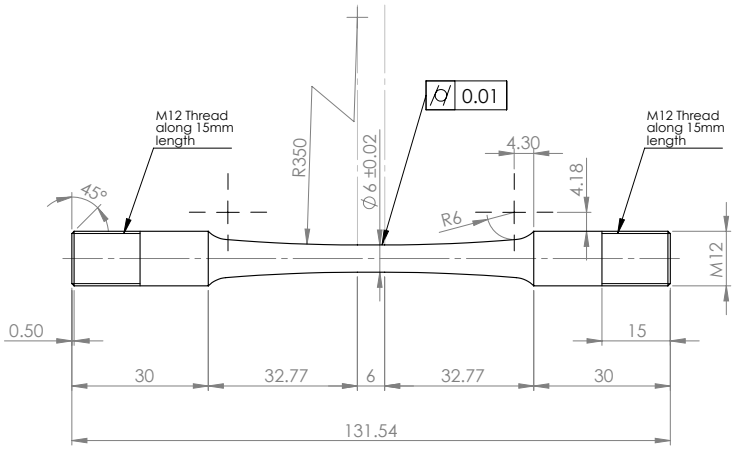

Figure 3: HGR6 specimen geometry.

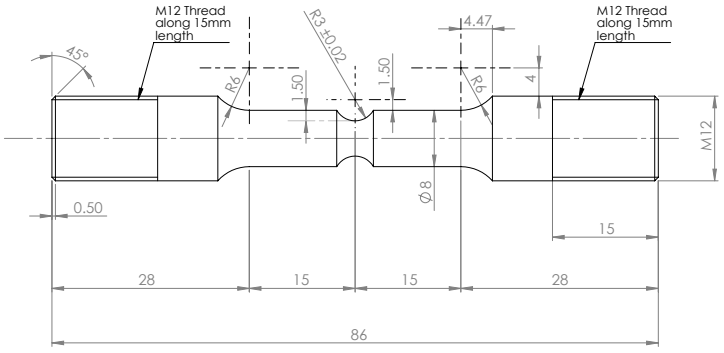

Figure 4: RNB6 specimen geometry ($a = 5$ mm, $\rho = 3$ mm).

Material	Geom.	Spec.	Imaging			Shadowgraph
			ε_{onset} [-]	ρ_f [mm]	a_f [mm]	a_f [mm]
s/s 304L	RB6	#14	0.35	2.62	1.50	1.49
		#16	0.38	2.58	1.51	1.53
copper C110	RB6	#1	0.05	0.94	1.29	1.27
		#2	0.05	0.88	1.22	1.22

Table 2: Neck onset strain (ε_{onset}), final neck radius of curvature (ρ_f) and final cross-sectional radius (a_f) measured with imaging method; final cross-sectional radius (a_f) measured with shadowgraph.

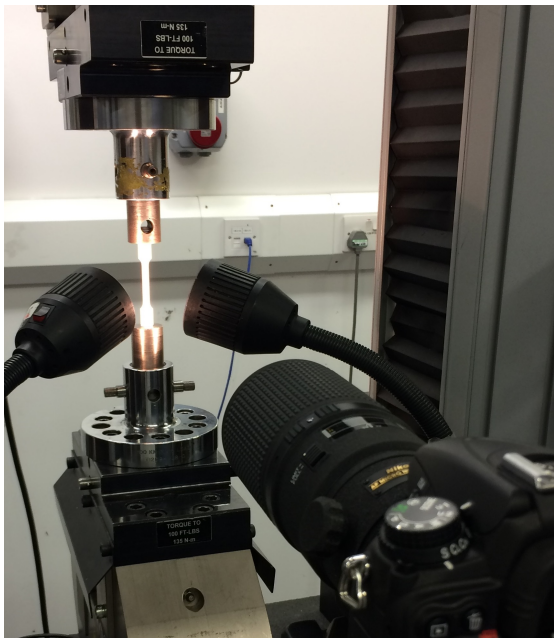

Figure 5: Experimental rig used for the specimen's neck geometry monitoring.

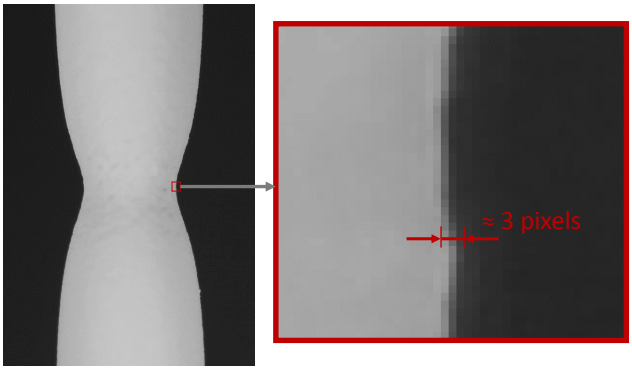

Figure 6: Representation of the accuracy of the neck monitoring technique, thickness of the grey transition between dark and light pixels of the image.

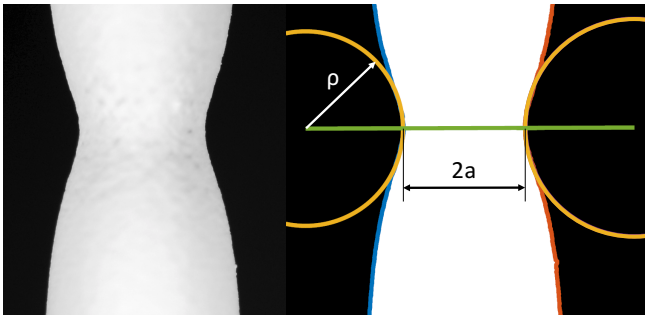

Figure 7: Representation of the necked specimen obtained in the condition of $\varepsilon_T = 1.3$ for a stainless steel 304L specimen. The neck shape, minimum diameter ($2a$) and osculating circles are shown.

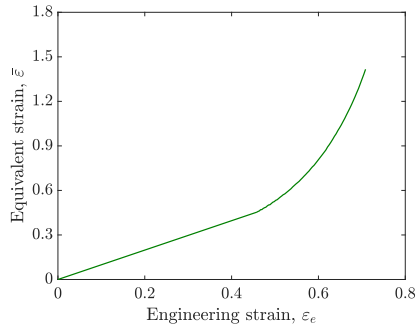

(a) Strain correction for stainless steel 304L

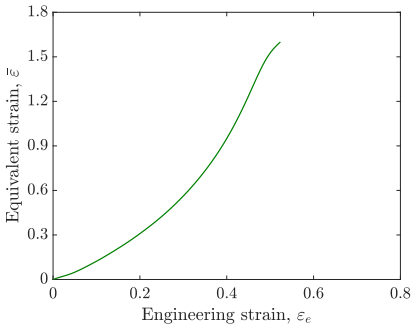

(b) Strain correction for copper C110

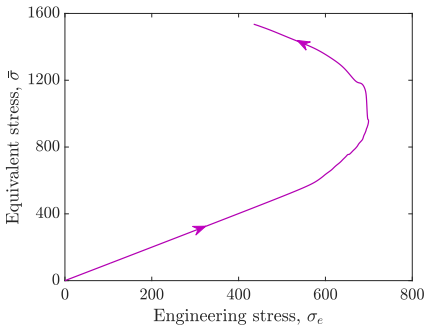

(c) Stress correction for stainless steel 304L

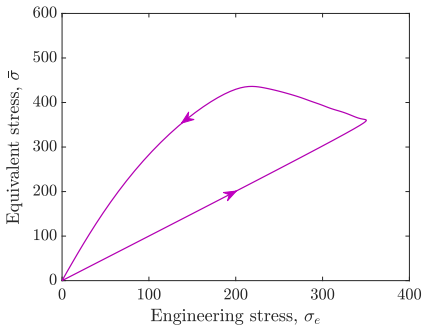

(d) Stress correction for copper C110

Figure 8: Necking effect correction curves: strain correction ($\bar{\varepsilon}$ - ε_e) and stress correction ($\bar{\sigma}$ - σ_e).

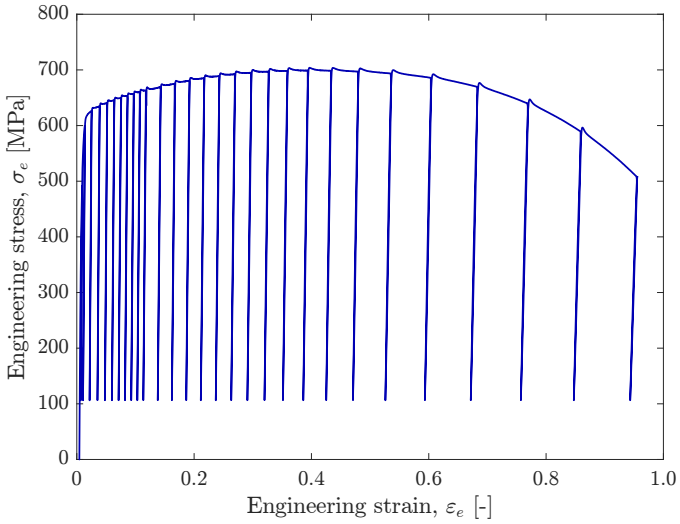

Figure 9: Engineering stress - engineering strain history of the elastic modulus monitoring test.

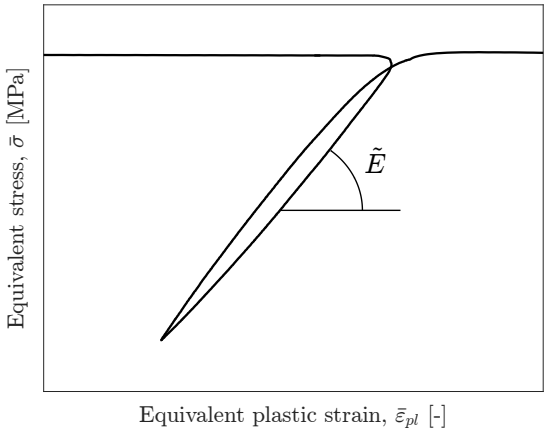

Figure 10: Equivalent stress - equivalent plastic strain ($\bar{\sigma}$ - $\bar{\varepsilon}_{pl}$) of one unloading-reloading cycle.

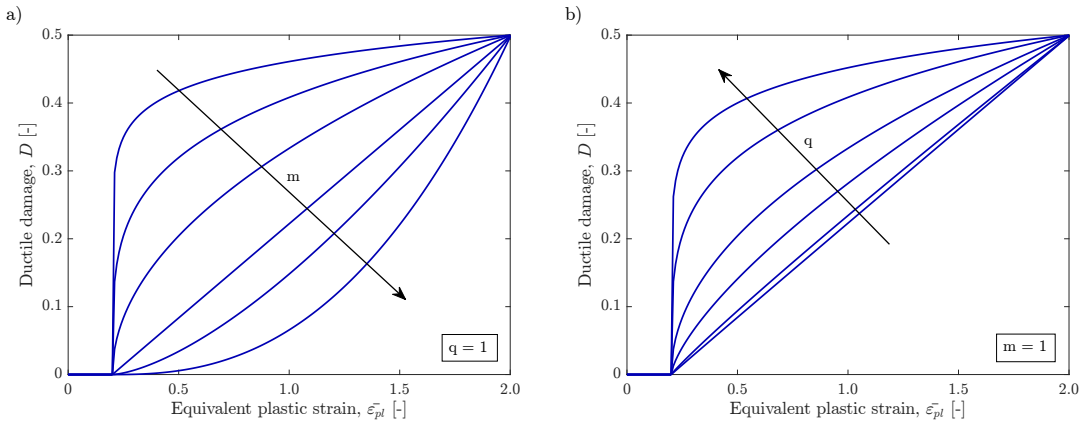

Figure 11: Effect of m and q parameters on the damage accumulation model: (a) $q = 1$ and variable m; (b) $m = 1$ and variable q. In both cases $\varepsilon_{th} = 0.2$ and $D_{cr} = 0.5$.

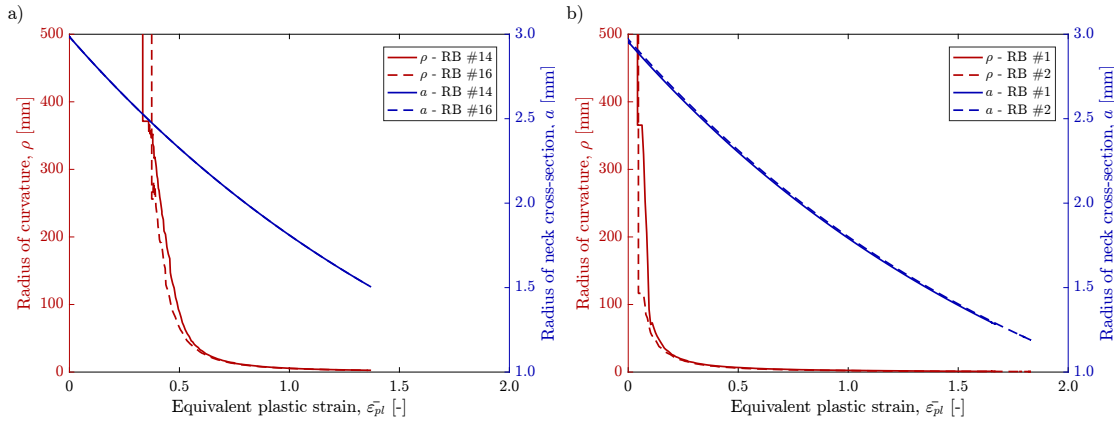

Figure 12: Evolution of the neck geometry (minimum cross-sectional radius (a) and radius of curvature of the osculating circle (ρ)) vs. equivalent plastic strain: (a) stainless steel 304L; (b) copper C110.

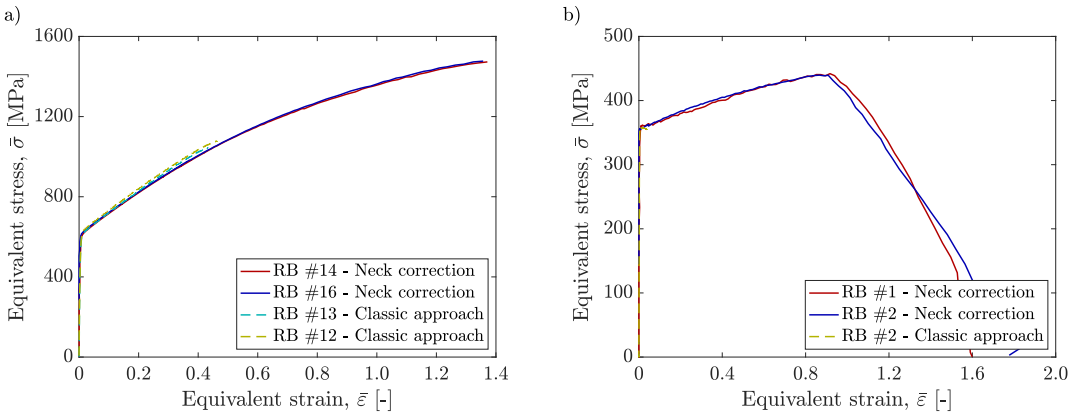

Figure 13: Equivalent stress - equivalent strain: (a) stainless steel 304L; (b) copper C110.

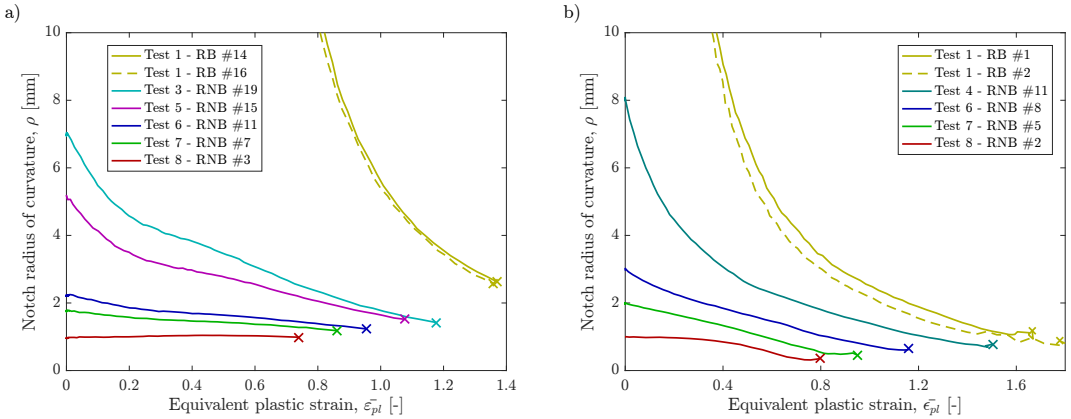

Figure 14: Evolution of the radius of curvature of the notch with applied equivalent plastic strain for the different RNB tensile tests: (a) stainless steel 304L; (b) copper C110.

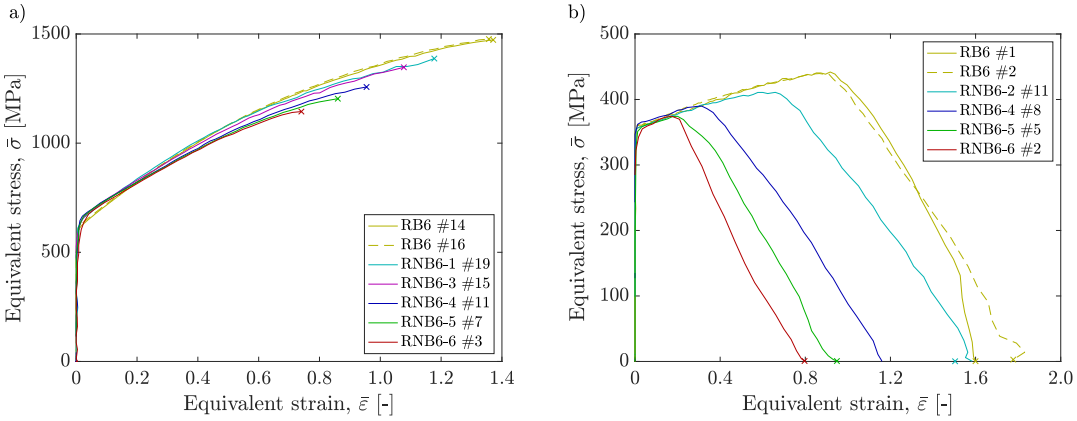

Figure 15: Equivalent stress - equivalent strain of the RNB tensile tests: (a) stainless steel 304L; (b) copper C110.

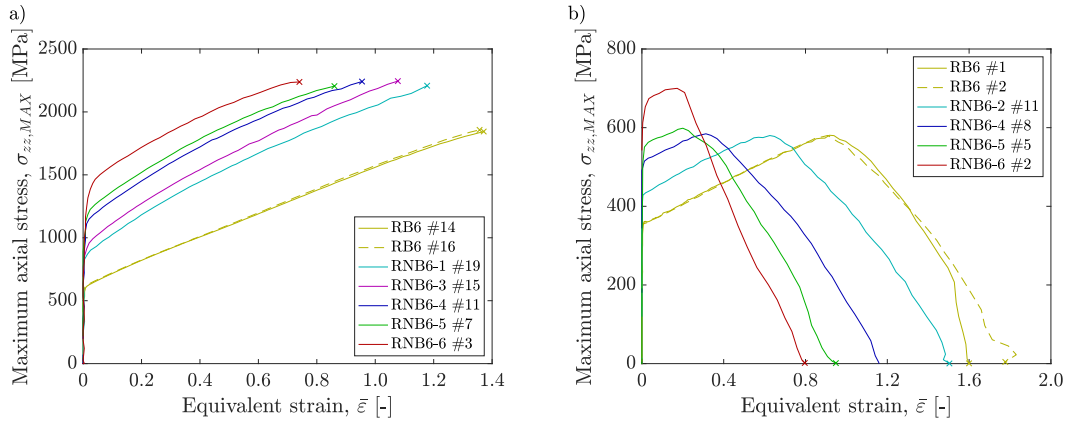

Figure 16: Maximum axial stress - equivalent strain of the RNB tensile tests: (a) stainless steel 304L; (b) copper C110.

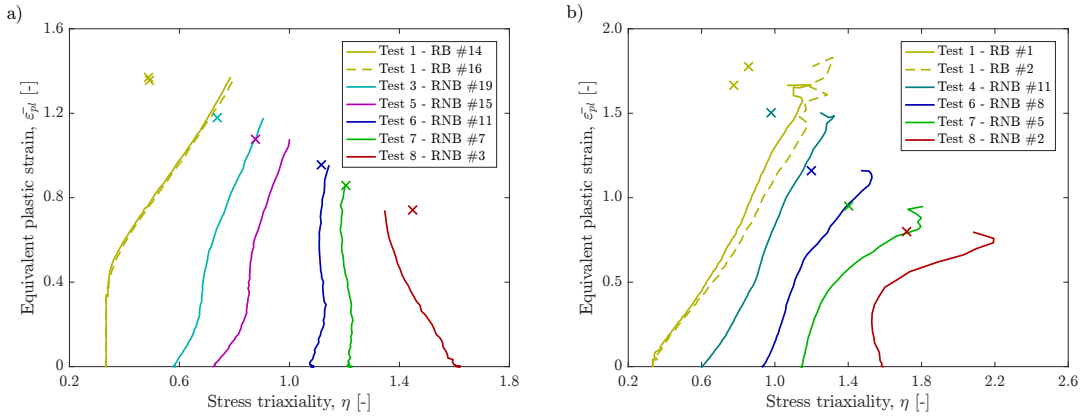

Figure 17: Variation of stress triaxiality with applied equivalent plastic strain for the different RNB tensile tests, the crosses represent the fracture equivalent plastic strain vs. average triaxiality ($\bar{\varepsilon}_{pl,f}$,η_{av}): (a) stainless steel 304L; (b) copper C110.

Test #	Notch acuity, a/ρ [-]	Spec.	Theor.	Imaging				Shadowgr.
			η_0	η_0	η_f	η_{av}	$\bar{\varepsilon}_f$	$\bar{\varepsilon}_f$
1	0	#14	0.333	0.333	0.787	0.491	1.37	1.39
		#16	0.333	0.333	0.796	0.494	1.36	1.34
3	0.25	#19	0.546	0.582	0.905	0.742	1.18	1.18
5	0.417	#15	0.660	0.726	1.001	0.880	1.08	1.04
6	0.833	#11	0.892	1.084	1.144	1.117	0.96	0.96
7	1.25	#7	1.110	1.225	1.203	1.207	0.86	0.88
8	2.5	#3	1.540	1.614	1.346	1.447	0.74	0.75

Table 3: Stress triaxiality results of stainless steel 304L. Theoretical initial stress triaxiality (η_0) obtained using Eq. 1; initial (η_0), final (η_f) and average (η_{av}) stress triaxiality throughout the test obtained using the proposed imaging method; and fracture equivalent strain ($\bar{\varepsilon}_f$) obtained using the imaging technique and measuring the final diameter.

Test #	Notch acuity, a/ρ [-]	Spec.	Theor.	Imaging				Shadowgr.
			η_0	η_0	η_f	η_{av}	$\bar{\varepsilon}_f$	$\bar{\varepsilon}_f$
1	0	#1	0.333	0.333	1.397	0.823	1.60	1.69
		#2	0.333	0.333	1.316	0.867	1.78	1.78
4	0.313	#11	0.606	0.602	1.324	0.981	1.50	1.49
6	0.833	#8	0.958	0.936	1.530	1.198	1.16	1.19
7	1.25	#5	1.173	1.147	1.808	1.403	0.95	0.98
8	2.5	#2	1.532	1.586	2.081	1.721	0.80	0.77

Table 4: Stress triaxiality results of copper C110. Theoretical initial stress triaxiality (η_0) obtained using Eq. 1; initial (η_0), final (η_f) and average (η_{av}) stress triaxiality throughout the test obtained using the proposed imaging method; and fracture equivalent strain ($\bar{\varepsilon}_f$) obtained using the imaging technique and measuring the final diameter.

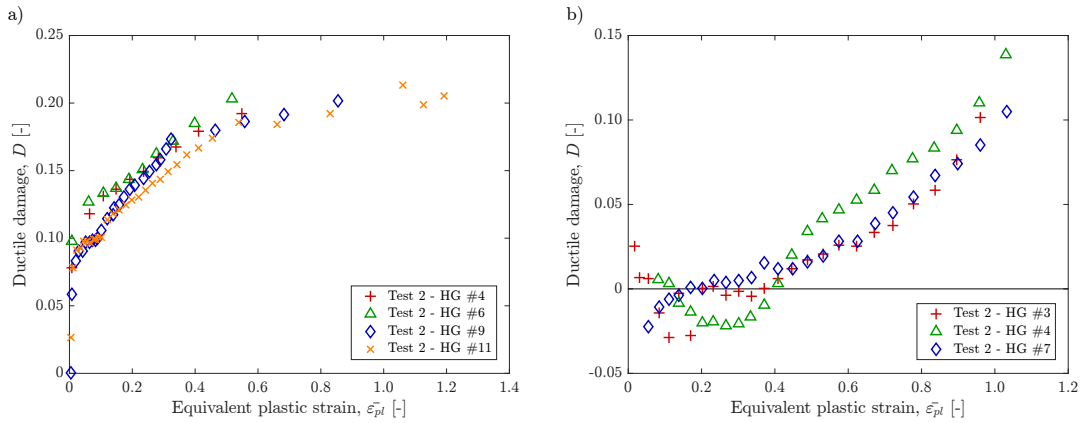

Figure 18: Ductile damage - equivalent plastic strain experimental results: (a) stainless steel 304L; (b) copper C110.

Specimen	#34	#33	#32	#36	#31	#6
Equivalent plastic strain ($\bar{\varepsilon}_{pl}$)	0.110	0.214	0.384	0.673	0.993	1.292

Table 5: Specimens studied in the metallographic damage analysis and equivalent plastic strains.

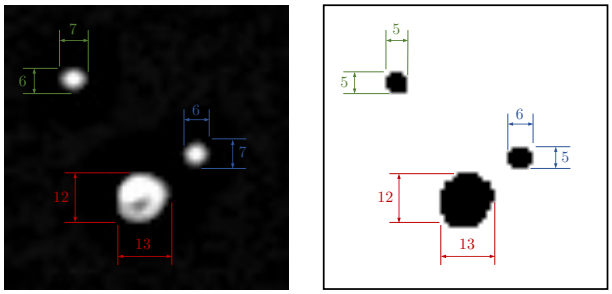

Figure 19: Size comparison of individual voids in the original and thresholded pictures for the calibration of the intensity threshold value; numbers represent size in pixels.

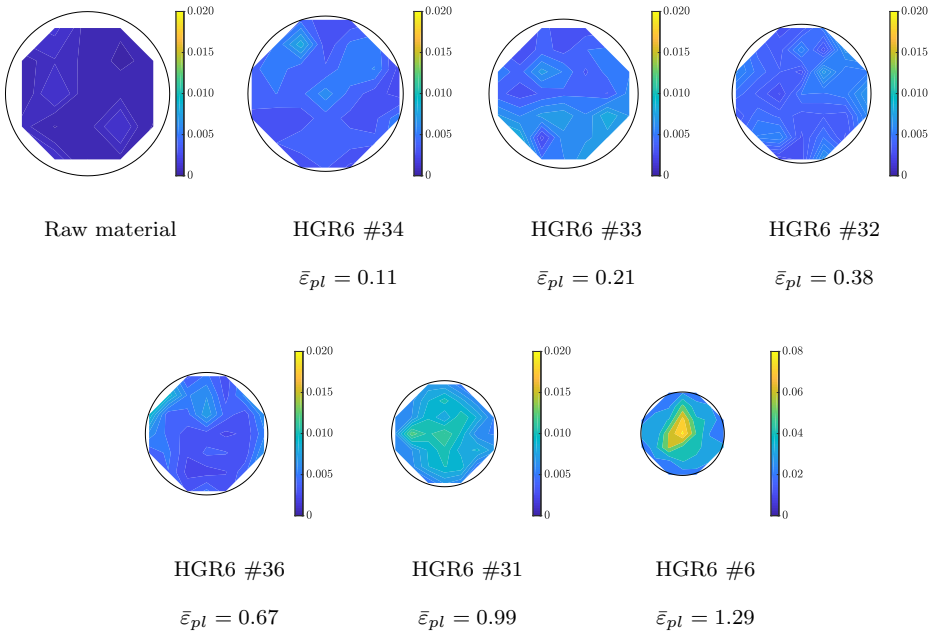

Figure 20: Contours of porosity in the cross-section of the analysed specimens.

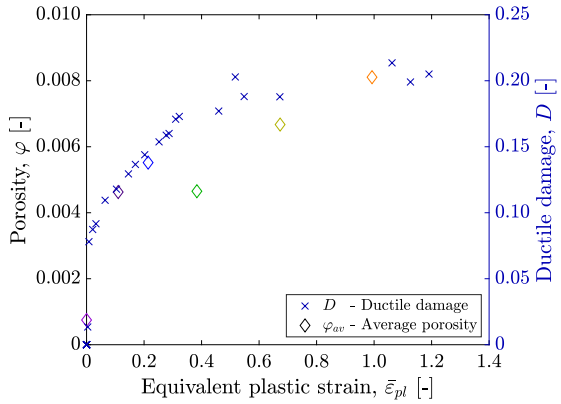

Figure 21: Analysis of the porosity and ductile damage evolution with equivalent plastic strain.

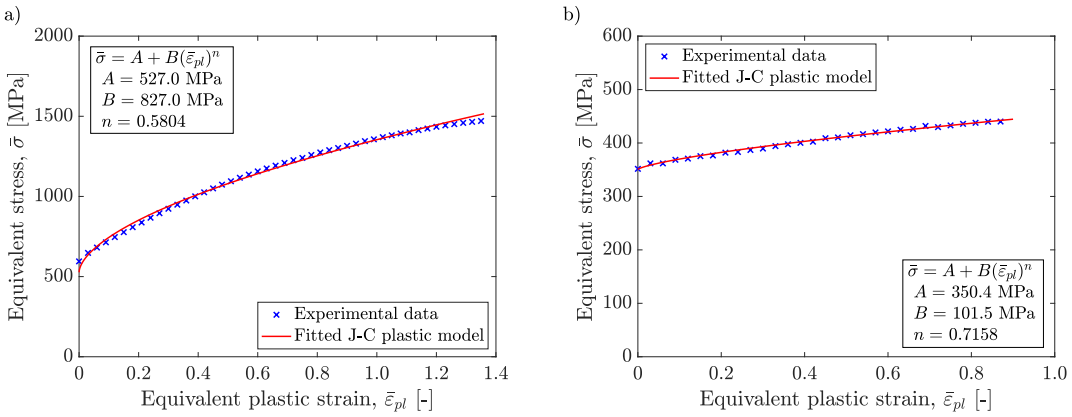

Figure 22: Experimental true equivalent stress - true equivalent plastic strain data fitted to Johnson-Cook plastic model: (a) stainless steel 304L; (b) copper C110.

Material	A [MPa]	B [MPa]	n
Stainless steel 304L	628.7	945.2	0.9314
Copper C110	354.1	259.2	0.9221

Table 6: Plastic model parameters.

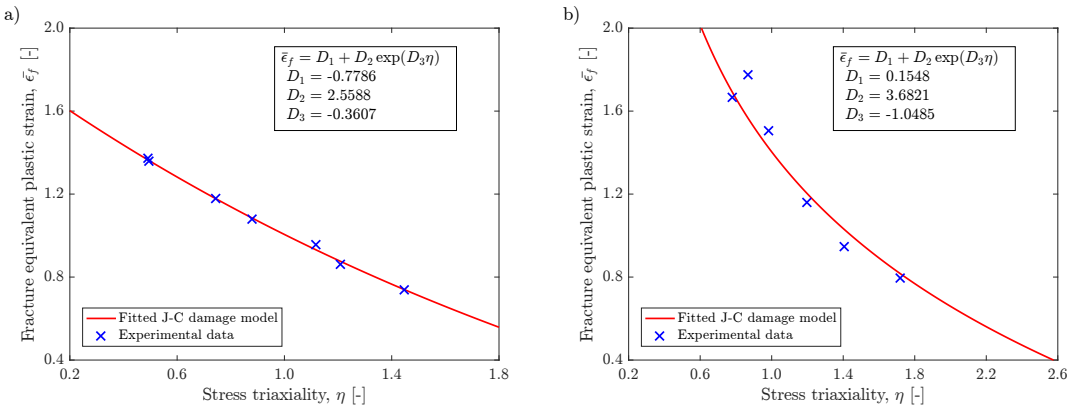

Figure 23: Experimental fracture equivalent plastic strain - stress triaxiality data fitted to Johnson-Cook fracture model: (a) stainless steel 304L; (b) copper C110.

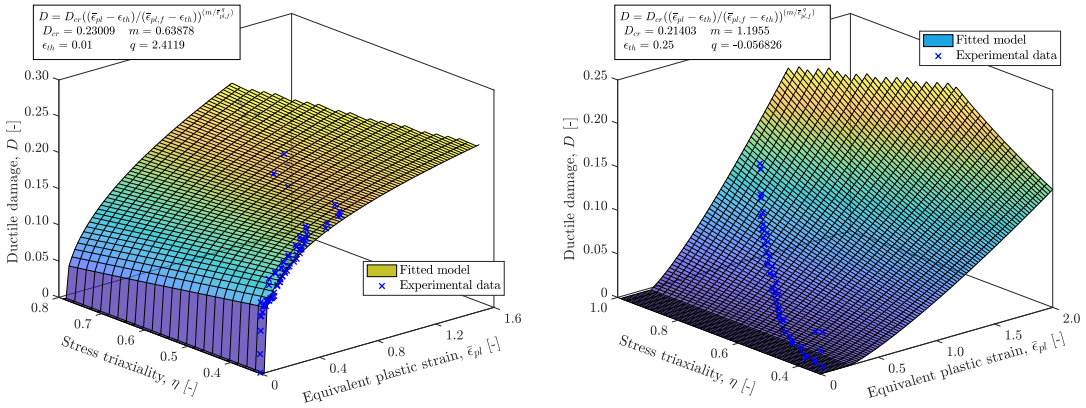

Figure 24: Experimental ductile damage as a function of equivalent plastic strain and stress triaxiality data fitted to the proposed damage accumulation model: (a) stainless steel 304L; (b) copper C110.

Material	D_1	D_2	D_3	D_{cr}	ε_{th}	m	q
Stainless steel 304L	-0.7786	2.5588	-0.3607	0.226	0.01	0.4115	1.3058
Copper C110	0.1548	3.6821	-1.0485	0.214	0.25	1.1955	-0.0568

Table 7: Fracture and damage accumulation model parameters.